A High Entropy Multicationic Substituted Lithium Argyrodite Superionic Solid Electrolyte

Jing Lin,[a] Gennady Cherkashinin,[b] Mareen Schäfer,[c] Georgian Melinte,[d] Sylvio Indris,[c,e] Aleksandr Kondrakov,[a,f] Jürgen Janek,[a,g] Torsten Brezesinski,[a*] and Florian Strauss[a*]

[a] Battery and Electrochemistry Laboratory (BELLA), Institute of Nanotechnology, Karlsruhe Institute of Technology (KIT), Hermann-von-Helmholtz-Platz 1, 76344 Eggenstein-Leopoldshafen, Germany.

[b] Institute for Materials Science, Technical University Darmstadt, Alarich-Weiss Str. 2, 64287 Darmstadt, Germany.

[c] Institute for Applied Materials–Energy Storage Systems, Karlsruhe Institute of Technology (KIT), Hermann-von-Helmholtz-Platz 1, 76344 Eggenstein-Leopoldshafen, Germany.

[d] Institute of Nanotechnology, Karlsruhe Institute of Technology (KIT), Hermann-von-Helmholtz-Platz 1, 76344 Eggenstein-Leopoldshafen, Germany.

[e] Helmholtz Institute Ulm (HIU) Electrochemical Energy Storage, Helmholtzstr. 11, 89081 Ulm, Germany.

[f] BASF SE, Carl-Bosch-Str. 38, 67056 Ludwigshafen, Germany.

[g] Institute of Physical Chemistry & Center for Materials Science (ZfM/LaMa), Justus-Liebig-University Giessen, Heinrich-Buff-Ring 17, 35392 Giessen, Germany.

Abstract

Bulk-type solid-state batteries (SSBs) constitute a promising next-generation technology for electrochemical energy storage. However, in order for SSBs to become competitive with mature battery technologies, (electro)chemically stable, superionic solid electrolytes are much needed. Multicomponent or high entropy lithium argyrodites have recently attracted much attention for their favorable material characteristics. In the present work, we report on increasing the configurational entropy of the $Li_{6+a}P_{1-x}M_xS_5I$ solid electrolyte system and examine how this affects the structure-conductivity/stability relationships. Using electrochemical impedance spectroscopy and ^7Li pulsed field gradient nuclear magnetic resonance (NMR) spectroscopy, multicationic substitution is demonstrated to result in a very low activation energy for Li diffusion of ~0.2 eV and a high room-temperature ionic conductivity of ~13 mS cm^{-1} (for $Li_{6.5}[P_{0.25}Si_{0.25}Ge_{0.25}Sb_{0.25}]S_5I$). The transport properties are rationalized from a structural perspective by means of complementary neutron powder diffraction and magic-angle spinning NMR spectroscopy measurements. The $Li_{6.5}[P_{0.25}Si_{0.25}Ge_{0.25}Sb_{0.25}]S_5I$ solid electrolyte was also tested in high-loading SSB cells with a Ni-rich layered oxide cathode and found by X-ray photoelectron

spectroscopy to suffer from interfacial side reactions during cycling. Overall, the results of this study indicate that optimization of conductivity is equally important to optimization of stability and compositionally complex lithium argyrodites represent a new playground for rational design of (potentially advanced) superionic solid electrolytes.

Lithium-ion batteries (LIBs) are one of the most advanced energy-storage technologies at this time.[1,2] The application of solid electrolytes (SEs) instead of conventional liquid electrolytes can potentially lead to significant leaps in cell energy density.[3–6] Among the different classes of inorganic SEs, lithium thiophosphates are considered most promising. This is due in part to their high ionic conductivity ($\sigma_{ion,\ r.t.} \geq 1$ mS cm^{-1}) and favorable mechanical properties, ensuring intimate contact between the key components in solid-state batteries (SSBs).[7–10] Especially lithium argyrodites with the general formula Li_6PS_5X (X = Cl, Br, I) are attracting much interest as potential high-performance SEs (with $\sigma_{ion,\ r.t.} \approx 2$ mS cm^{-1} for Li_6PS_5Cl).[11–14] These materials consist of $[PS_4]^{3-}$ structural units and free X^- and S^{2-} ions, offering a framework for fast lithium diffusion.[14,15] The ionic conductivity of lithium argyrodites has been increased by about an order of magnitude via substitution (primarily) on the phosphorus site. This kind of improvement is generally attributed to changes in the Li sublattice, with occupation of “additional” sites[16–19] and/or increased S^{2-}/X^- site inversion, such as in the case of $Li_{6.6}Si_{0.6}Sb_{0.4}S_5I$ (~15 and 24 mS cm^{-1} for cold-pressed and sintered pellets, respectively) and $Li_{6.6}P_{0.4}Ge_{0.6}S_5I$ (~6 and 18 mS cm^{-1} for cold-pressed and sintered pellets, respectively).[16,20–22] Recently, it has been shown that multianionic substituted lithium argyrodites do not possess increased ionic conductivity, although the activation energy for conduction strongly decreased.[23] Multielement (equimolar) substitution, specifically having more than five elements sharing a single crystallographic site, refers to so-called high entropy materials (HEMs) with $\Delta S_{config} \geq 1.5R$.[24] Note that ΔS_{config} represents the configurational entropy and can be calculated as detailed in the Supporting Information. In the past years, the concept of HEMs has been extended from high entropy alloys to different oxide-, carbide-, and sulfide-based materials.[25–29] HEMs often show new or improved properties over their low entropy counterparts and have been applied in various fields, e.g. as thermoelectric materials or battery electrodes.[30–39] As mentioned above, high configurational entropy in lithium argyrodites, with a ΔS_{config} of up to $2.98R$, could so far only be achieved through predominantly anionic mixing.[23] Multicationic substitution for increasing the configurational entropy and how this affects the structure-property relationships related to charge transport and electrochemical stability has not yet been explored. In the present work, we report on the synthesis and characterization of a multicationic substituted lithium argyrodite SE.

After screening a variety of cation species for substituting phosphorus in Li_6PS_5I (in an equimolar manner), we successfully synthesized $Li_{6.5}[P_{0.25}Si_{0.25}Ge_{0.25}Sb_{0.25}]S_5I$ by high-energy milling and post annealing at 500 °C in a vacuum-sealed quartz ampule

(see Supporting Information for details on the preparation and **Table S1** for other compositions targeted in the synthesis). Assuming equal distribution of elements over the different crystallographic sites, ΔS_{config} was calculated to be 2.77*R*, rendering it a high entropy material. The respective X-ray diffraction (XRD) pattern showed reflections that could be assigned to a cubic argyrodite structure (**Figure S1**). The chemical composition was probed using inductively coupled plasma-optical emission spectroscopy (ICP-OES, see **Table S2**) and found to agree well with the target stoichiometry.

Neutron powder diffraction (NPD) was conducted on the sample at *T* = 298 K and 10 K to gain more insight into the crystal structure. The room-temperature NPD pattern and corresponding Rietveld refinement profile are shown in **Figure 1a**. The pattern was indexed in the *F*−43*m* space group, with lattice parameter *a* = 10.29714(9) Å, resulting in a cell volume of *V* = 1091.816(2) Å^3. More detailed structural information is provided in **Table S3**. For minimizing atomic thermal displacement, NPD was also performed at *T* = 10 K. As shown in **Figure 1b**, a similar pattern to that obtained at 298 K was observed. In line with expectations, Rietveld analysis revealed a smaller lattice parameter (10.24932(5) Å) and cell volume (1076.677(10) Å^3), see **Table S4** for details. Interestingly, unlike Li_6PS_5I, the multicationic substituted argyrodite did not show a polymorphic phase transition at low temperatures.[15] The calculated crystal structure of $Li_{6.5}[P_{0.25}Si_{0.25}Ge_{0.25}Sb_{0.25}]S_5I$ is depicted in **Figure 1c**. Both the S^{2-} and I^- ions form a face centered cubic sublattice (Wyckoff positions 4*a* and 4*d*). In addition, the S^{2-} ions are situated in half of the tetrahedral voids (Wyckoff position 16*e*) around the octahedral sites (central atom on Wyckoff position 4*b*), forming the multianionic $[P_{0.25}Si_{0.25}Ge_{0.25}Sb_{0.25}S_4]^{3.5-}$ tetrahedra (constituting a combination of $[PS_4]^{3-}$, $[SiS_4]^{4-}$, $[GeS_4]^{4-}$, and $[SbS_4]^{3-}$).

To further corroborate the local tetrahedral environment of P and Si, ^{31}P and ^{29}Si magic-angle spinning (MAS) nuclear magnetic resonance (NMR) spectroscopy measurements were carried out. A distinct peak centered at 91.2 ppm was observed in the ^{31}P MAS NMR spectrum (**Figure 1d**), indicative of $[PS_4]^{3-}$ and consistent with the ^{31}P chemical shift reported for other lithium thiophosphates.[23,40,41] Compared to Li_6PS_5I, the ^{31}P signal was shifted by ~5 ppm,[14] which is probably a result of the unique chemical environment. Regarding the ^{29}Si signal, a sharp peak appeared at a chemical shift of 11.5 ppm (**Figure 1e**), in agreement with the study on LGPS-like Li_7SiPS_8 (with $[SiS_4]^{4-}$ units) by Lotsch and coworkers.[40] Note that the sharp ^{31}P and ^{29}Si MAS NMR signals suggest a relatively low degree of next-neighbor disorder, which was not the case for other types of multicomponent lithium argyrodites.[14,23] In particular, the atoms located on 4*a* (halide) and 4*d* (sulfide) are known to distribute over both crystallographic sites. For $Li_{6.5}[P_{0.25}Si_{0.25}Ge_{0.25}Sb_{0.25}]S_5I$, we observed a S^{2-}/I^- site inversion of 11 %, which is relatively high considering the mismatch in ionic radii. Taking into account both the equal distribution of elements on the 4*b* site (tetrahedral environment) and the aforementioned site inversion (Wyckoff positions 4*a* and 4*d*), ΔS_{config} was calculated to be 2.03*R*, rendering $Li_{6.5}[P_{0.25}Si_{0.25}Ge_{0.25}Sb_{0.25}]S_5I$ a true high entropy material.

Apart from the disorder, detailed information about the Li sublattice was obtained from Rietveld analysis of the NPD data. The mobile Li atoms are known to form Frank-Kasper polyhedra in the argyrodite structure. They are usually distributed around the 4*d* site over two Wyckoff positions, namely 48*h* and 24*g*.[14] For $Li_{6.5}[P_{0.25}Si_{0.25}Ge_{0.25}Sb_{0.25}]S_5I$, 38 and 62 % were found on 24*g* and 48*h*, respectively, at room temperature (**Figure S2**). The Li occupancy remained virtually unaltered upon decreasing the temperature to T = 10 K. Such a large fraction of Li located on the intermediate/transition 24*g* site caused strong Coulomb repulsion between the two neighboring 48*h* sites,[21] eventually resulting in an enlarged 48*h*-48*h* doublet jump distance of 1.39 Å, compared to 1.25 Å for Li_6PS_5I (**Table S5**). This in turn led to decreased intercage jump distances of 3.24 Å, favoring facile long-range lithium diffusion.

The particle morphology and elemental distribution were probed using high-angle annular dark-field scanning transmission electron microscopy (HAADF STEM) and energy-dispersive X-ray spectroscopy (EDS). The average primary particle size was found to be larger than 1 µm (**Figure 1e**), and the EDS maps indicated uniform distribution on the sub-micrometer level (i.e. accumulation/segregation of individual elements can be ruled out).

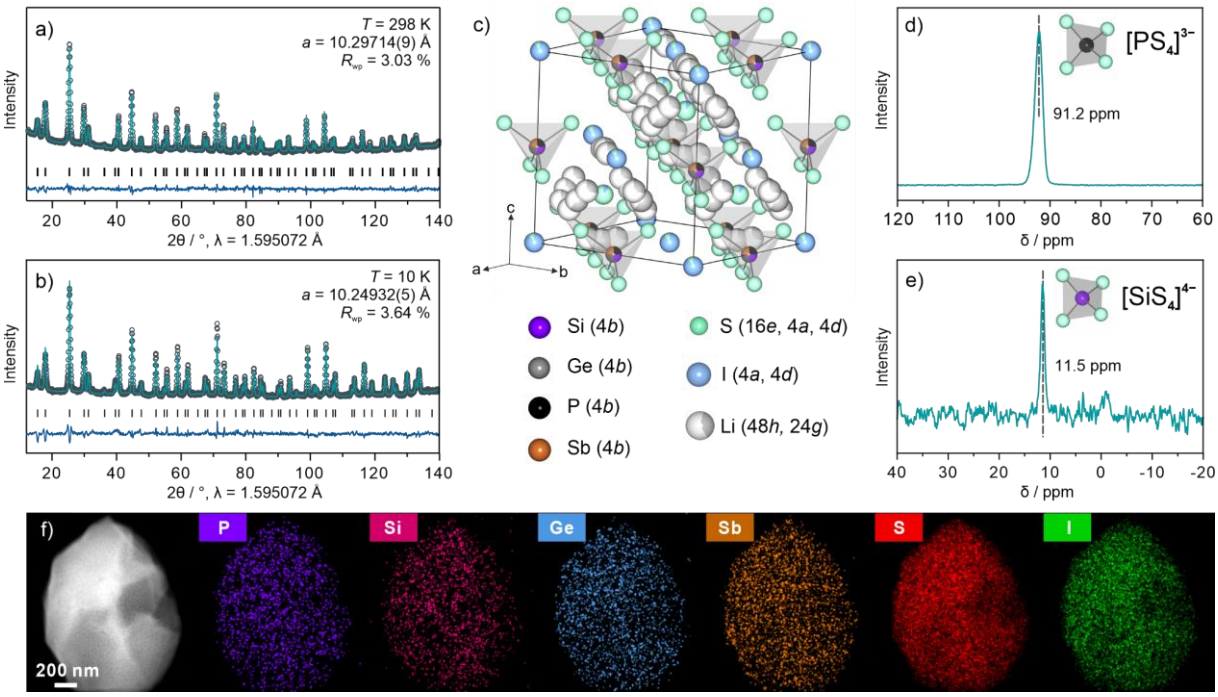

Figure 1. (a-e) Structural characterization of $Li_{6.5}[P_{0.25}Si_{0.25}Ge_{0.25}Sb_{0.25}]S_5I$. NPD patterns collected at (a) T = 298 K and (b) 10 K and corresponding Rietveld refinement plots. The observed, calculated, and difference profiles are shown as gray circles, cyan lines, and blue lines, respectively. Vertical tick marks denote the expected Bragg reflections. (c) Crystal structure with the different elements and Wyckoff positions indicated in the legend. (d) ^{31}P and (e) ^{29}Si MAS NMR spectra. (f) HAADF STEM image and corresponding EDS maps.

To gain information about the oxidation state of the different elements, X-ray photoelectron spectroscopy (XPS) measurements were conducted on the $Li_{6.5}[P_{0.25}Si_{0.25}Ge_{0.25}Sb_{0.25}]S_5I$ sample. For the Sb 3d core-level region, only the $3d_{5/2}$ component is shown in **Figure 2a**, due to large spin-orbit splitting (~9.3 eV). The Sb $3d_{5/2}$ spectrum was superimposed by the O1s signal at a binding energy of $E_{bin} \approx 532.5$ eV. The asymmetry of the Sb $3d_{5/2}$ component to low E_{bin} indicated two oxidation states, 529.5 eV for Sb^{3+} and 530.4 eV for Sb^{5+}, confirming the Sb-S chemical environment in the surface region.[42–45] The O1s peak was asymmetric to high E_{bin}, suggesting the presence of at least two chemical states, at 532.0 and 532.9 eV (**Figure 2a**). These states can probably be attributed to oxygenated Si, Sb, P, and/or Ge. However, clear assignment is challenging. It should be noted that the formation of Sb-O species, due to oxygen contamination, cannot be fully ruled out. For example, the Sb $3d_{5/2}$ peak of Sb_2O_5 is expected to appear at $E_{bin} > 531$ eV.[42] Fitting of the Sb $3d_{3/2}$ region also revealed two oxidation states, at E_{bin} = 538.9 (Sb^{3+}) and 539.8 eV (Sb^{5+}) (**Figure S3**). Overall, we attribute the Sb^{5+} contribution to Sb in $[SbS_4]^{3-}$, while the Sb^{3+} presumably stems from not fully oxidized surface impurities, despite using excess sulfur in the synthesis. The S 2p detail spectrum is shown in **Figure 2b**. The E_{bin} of 161.6 eV assumes the presence of sulfid species, in agreement with available literature reports on lithium thiophosphates.[46–48] **Figure 2c** displays the P 2p core-level region. Only a single component was detected at E_{bin} = 132.4 eV, which can be assigned to the $[PS_4]^{3-}$ units.[46–48] The binding energy was slightly higher compared with related thiophosphate SEs (~131.9 eV). We assume that the shift in E_{bin} results either from the different chemical environment (compositional disorder) or the formation of partially oxygenated P species. **Figure 2d** shows the Si 2p detail spectrum. The main feature at E_{bin} = 101.1 eV can be assigned to $[SiS_4]^{4-}$, as observed for lithium thiosilicates.[49,50] This finding agrees with the structural characterization results. The binding energy of the minor Si 2p component (E_{bin} = 103.3 eV) was slightly higher than that of free SiS_2.[49,50] It probably stems from SiO_x impurities,[51,52] since lithium thiophosphate surfaces are known to be very reactive toward oxygen-containing species. The I 4d region (~2.0 eV spin-orbit splitting) indicated the presence of two chemical states, at 49.3 and 49.9 eV, associated with the I^- species (**Figure 2e**). The I $3d_{5/2}$ data in **Figure S4** corroborate this result.[53,54] We hypothesize that the two chemical states result from the different crystallographic sites, with different local chemical environments, occupied by I^- (Wyckoff positions 4*a* and 4*d*, with ~89 and 11 % I^-, respectively). The Ge 3d and Sb 4d regions are shown in **Figure 2f**. The Sb 4d peaks (~1.3 eV spin-orbit splitting) were situated at slightly higher E_{bin} from the Ge 3d photoemission. Their shape (i.e. two chemical states with E_{bin} = 33.3 and 34.3 eV due to Sb^{3+} and Sb^{5+}, respectively, with Sb-S environment) supports the discussion above on the Sb $3d_{5/2}$ spectrum.[42,43] The Ge 3d spectrum revealed a single component at E_{bin} = 30.9 eV. The latter binding energy refers to $[GeS_4]^{4-}$ (30.8-30.9 eV)[42,55] and is much lower than that expected for GeO_2 (32.4-32.5 eV).[56,57] Thus, the presence of oxygenated Ge is rather unlikely.

The XPS and structural analysis results collectively provide evidence that the bulk material adopts an argyrodite-type structure. However, we found slight deviations in chemical composition and state of selected elements in the surface region. Especially antimony seems to exist in mixed oxidation states and the presence of oxygenated species (most pronounced for SiO_x) was observed, despite the material processing under inert atmosphere conditions. Nevertheless, some undesirable side reactions with trace water/oxygen and/or precursor impurities throughout handling/data collection cannot be ruled out. The results obtained from quantitative XPS analysis are shown in **Table S6**. Considering the typical error, they agree reasonably well with the theoretical composition.

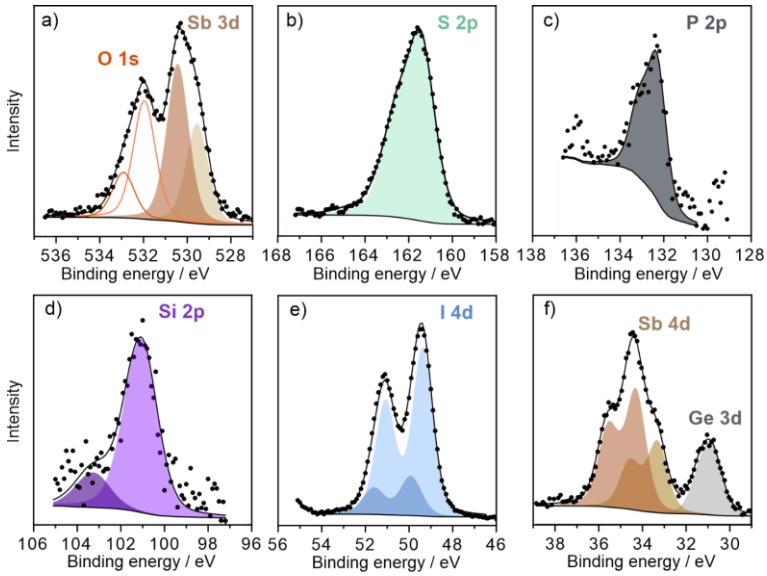

Figure 2. High-resolution (a) Sb $3d_{5/2}$ and O 1s, (b) S 2p, (c) P 2p, (d) Si 2p, (e) I 4d, and (f) Sb 4d and Ge 3d photoelectron spectra collected from $Li_{6.5}[P_{0.25}Si_{0.25}Ge_{0.25}Sb_{0.25}]S_5I$. Black circles and lines represent the experimental data and curve-fitting results, respectively.

After characterization of the bulk/surface structure, the Li-ion dynamics were probed using both ^{7}Li pulsed field gradient (PFG) NMR spectroscopy and electrochemical impedance spectroscopy (EIS). ^{7}Li PFG NMR spectroscopy was used to determine the diffusion coefficient D_{Li} in the temperature range of 30-70 °C and the activation energy E_A for Li diffusion (**Figure S5**). D_{Li} was found to be $7.09 \cdot 10^{-12}$ m^2 s^{-1} at ϑ = 30 °C, similar to other thiophosphate superionic conductors with a high Li diffusivity.[58–60] The Arrhenius plot of diffusivity versus T^{-1} is shown in **Figure 3a**, with E_A = (0.20 ± 0.01) eV determined from the slope. The electrical conductivity was measured by EIS on sintered pellets using ion-blocking indium electrodes. The Nyquist plots of the electrochemical impedance in the temperature range of 15-65 °C only showed a capacitive tail, suggesting high ion mobility (**Figure S6**). A room-temperature conductivity of 13.2 mS cm^{-1} was calculated from the data. As shown in **Figure 3b**, the temperature dependence of the conductivity followed an Arrhenius-type behavior,

with a similar activation energy E_A = (0.19 ± 0.01) eV to that determined by ^{7}Li PFG NMR spectroscopy. In addition, the ionic conductivity was calculated from the D_{Li} using the Nernst-Einstein equation (**Figure 3b**). It was found to be slightly lower than that from the EIS measurements (for a given temperature). However, the activation energies were virtually identical. We believe that the differences in conductivity are due to the presence of trace impurities (segregated at the grain boundaries), see previous section on XPS. The electronic conductivity was determined by DC polarization experiments to be 1.52 · 10^{-7} S cm^{-1} at room temperature (**Figure S7**), which is two to three orders of magnitude higher compared to related Li-ion conductors.[58,61,62] We hypothesize that this is due, in part, to the presence of Sb-based surface impurities showing mixed oxidation states.

Overall, the multicationic substituted $Li_{6.5}[P_{0.25}Si_{0.25}Ge_{0.25}Sb_{0.25}]S_5I$ was found to exhibit a very high ionic conductivity, with an activation energy for conduction that is among the lowest reported to date for lithium argyrodites (**Table S7**),[16,20,42] rendering it a promising material for bulk-type SSB applications.

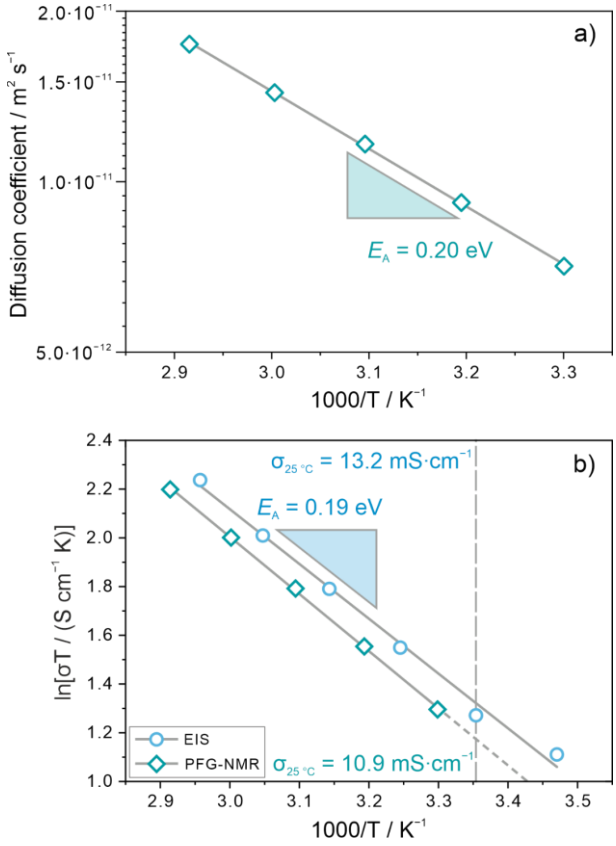

Figure 3. (a) Arrhenius plot of D_{Li} versus T^{-1}. (b) Ionic conductivity determined from EIS and ^{7}Li PFG NMR spectroscopy using the Nernst-Einstein equation. The room-temperature conductivities and activation energies are indicated.

The electrochemical behavior of $Li_{6.5}[P_{0.25}Si_{0.25}Ge_{0.25}Sb_{0.25}]S_5I$ as superionic SE was tested in pellet-stack SSBs with $LiNbO_3$-coated NCM851005 (85 % Ni content) and LTO ($Li_4Ti_5O_{12}$) as cathode and anode, respectively (see Supporting Information for

details on the electrode preparation and cell assembly). The charge/discharge cycling was performed between 1.35 and 2.75 V versus $Li_4Ti_5O_{12}/Li_7Ti_5O_{12}$ (approx. 2.9-4.3 V versus Li^+/Li) at a rate of C/2 and 25 °C (**Figure 4**). First-cycle specific charge and discharge capacities of 204 mAh g^{-1} (~2.3 mAh cm^{-2}) and 151 mAh g^{-1} (~1.7 mAh cm^{-2}) were achieved, corresponding to a Coulomb efficiency of 74 % (**Figure 4a**). In the 5th cycle, the SSB cell delivered a specific discharge capacity of 148 mAh g^{-1}, and the Coulomb efficiency increased to 98.4 %. Because of the high ionic conductivity of $Li_{6.5}[P_{0.25}Si_{0.25}Ge_{0.25}Sb_{0.25}]S_5I$, the cell was also subjected to rate performance testing from C/2 to 2C. As can be seen from **Figure 4b**, it was capable of delivering specific discharge capacities of ~118 and 72 mAh g^{-1} at 1C and 2C, respectively. On further cycling at C/2, the reversible capacity decayed to ~100 mAh g^{-1} (~1.1 mAh cm^{-2}) after 200 cycles, while the Coulomb efficiency stabilized close to 100 %. Although a surface-protected cathode active material (CAM) was employed in the present work, especially the first-cycle efficiency was relatively low, indicating that detrimental side reactions (i.e. (electro)chemical SE decomposition) occurred at the CAM|SE and carbon black|SE interfaces. In addition, the fairly linear capacity fading upon long-term cycling points toward continuous SE degradation, meaning it seems unlikely to form stable interfaces and interphases in this kind of battery system.

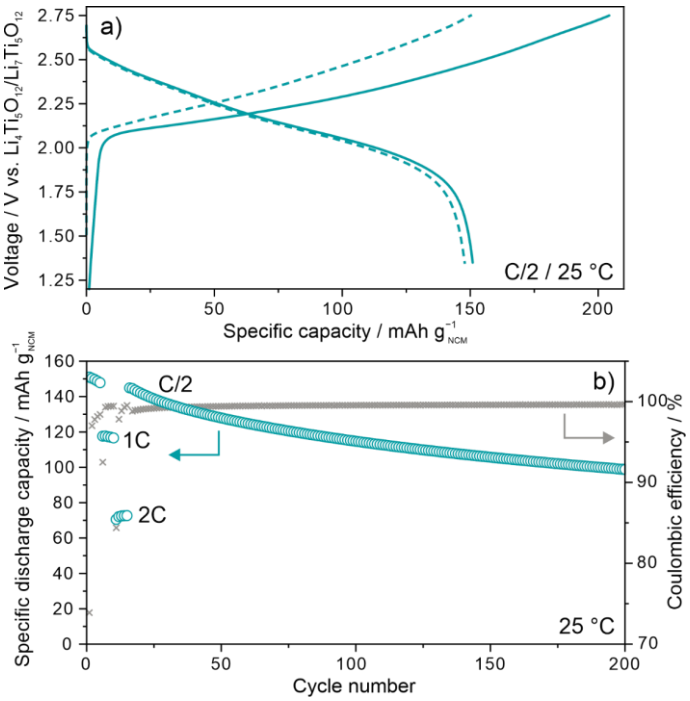

Figure 4. (a) Initial (solid line) and 5th-cycle (dashed line) voltage profiles of an SSB cell at C/2 rate and 25 °C. (b) Capacity retention and Coulomb efficiency over 200 cycles.

Ex situ XPS measurements were conducted on the cathode after cycling to learn more about the SE decomposition. The asymmetry of the Sb $3d_{5/2}$ component (**Figure 5a**) again indicated two oxidation states, 530.1 eV for Sb^{3+} and 530.8 eV for Sb^{5+}. The

latter E_{bin} were similar to those observed for the pristine material (**Figure 2a**), but with the major difference that the intensity of the Sb^{3+} component was strongly increased, suggesting Sb^{5+} reduction during electrochemical cycling. The shape of the O 1s core-level region also changed significantly (increase in intensity of the high binding-energy features at 531.9 and 532.9 eV, as well as appearance of a new component at 533.7 eV), due to the formation of oxygenated species (**Figure 5a**). This is also reflected in the increased amount of surface oxygen, as determined by quantitative XPS (**Table S6**). The S 2p spectrum indicated that the sulfur is strongly involved in the degradation of the SE (**Figure 5b**). Apart from the component at E_{bin} = 161.6 eV observed for the pristine material (**Figure 2b**), two new intense features appeared at E_{bin} = 162.2 and 163.5 eV. These components can be attributed to oxidized sulfur species (polysulfides), which usually have a broad binding-energy range depending on the chain length, gradually approaching the E_{bin} of elemental sulfur (163.5 eV).[46,63] The SSB cycling further led to the appearance of an additional peak at E_{bin} = 134.0 eV in the P 2p detail spectrum (**Figure 5c**), not present in **Figure 2c**. This component can be assigned to PO_x species (metal phosphates and/or metaphosphates),[46,48,64] the formation of which is commonly observed in thiophosphate-based SSBs upon cycling. The Si 2p spectrum showed an intense peak at 103.3 eV with some minor asymmetry to low E_{bin}, indicating another chemical state at E_{bin} = 101.5 eV (**Figure 5d**). Both components were also detected prior to cycling (**Figure 2d**), the difference being that the higher binding-energy peak increased strongly in intensity.[51,52] It is known that Ni-rich NCM CAMs release lattice oxygen during charge because of structural instabilities (incl. electrochemical oxidation of surface carbonates). The evolved oxygen can undergo follow-up reactions with thiophosphate SEs, thus being responsible, at least to some degree, for the formation of oxygenated decomposition products.[65–68] Note that the NCM851005 CAM was the only oxygen source in the cathode. However, chemical reactions with the protective surface coating cannot be ruled out. **Figure 5e** shows the I 4d core-level region of the SE after cycling. No major differences to the spectrum shown in **Figure 2e** were found. The variation in peak intensities (see also I $3d_{5/2}$ data in **Figure S4**) might be due to slight changes in local structural disorder. The Sb 4d and Ge 3d regions are shown in **Figure 5f**. The Ge 3d detail spectrum showed a single peak, but ~1 eV higher in binding energy than for the pristine material (31.8 eV vs. 30.9 eV). This is indicative of the presence of partially oxygenated Ge species (the E_{bin} lies between that of materials with $[GeS_4]^{4-}$ structural units and GeO_2). Similar to the pristine SE, the Sb 4d spectrum revealed the presence of Sb^{3+} and Sb^{5+}, with E_{bin} = 33.9 and 35.1 eV, respectively (**Figure 5f**). The shift toward higher binding energies was accompanied by an increase in intensity of the Sb^{3+} component because of Sb^{5+} reduction upon SSB operation (note that the Sb 3d data in **Figure 5a** show the same trend).

The XPS results clearly demonstrate that the $Li_{6.5}[P_{0.25}Si_{0.25}Ge_{0.25}Sb_{0.25}]S_5I$ SE in the composite cathode underwent adverse side reactions during cycling. Except for both phosphorus and iodine, all other elemental constituents were involved in the reactions. Especially silicon, sulfur, and antimony seem to be highly susceptible to oxygenation,

oxidation, and reduction, respectively. We note that the (electro)chemical reduction of Sb^{5+} to Sb^{3+} might be correlated with the oxidation of S^{2-}, leading to some kind of internal (irreversible) redox process, as also observed for other lithium thiophosphates.[69,70]

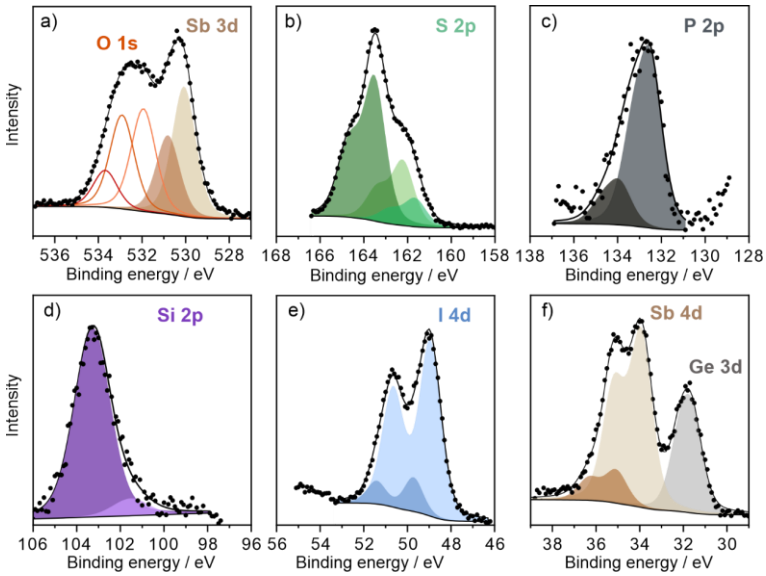

Figure 5. High-resolution (a) Sb $3d_{5/2}$ and O 1s, (b) S 2p, (c) P 2p, (d) Si 2p, (e) I 4d, and (f) Sb 4d and Ge 3d photoelectron spectra of $Li_{6.5}[P_{0.25}Si_{0.25}Ge_{0.25}Sb_{0.25}]S_5I$ after SSB cycling (200 cycles at C/2 rate and 25 °C). Black circles and lines present the experimental data and curve-fitting results, respectively.

In summary, we have successfully synthesized a compositionally complex lithium argyrodite SE by partially substituting phosphorus with other elements in an equimolar manner. The material showed a high ionic conductivity at room temperature (~13 mS cm^{-1}), along with very low activation energy for conduction (~0.2 eV), similar to the best-performing lithium argyrodites reported so far (**Table S7**). The properties arise from distinct structural features induced by the multicationic substitution. High S^{2-}/I^- site inversion was achieved (11 %, among the highest values reported in the literature for $Li_{6+a}P_{1-x}M_xS_5I$ materials),[16,21] which has been shown to energetically facilitate intercage jumps and to be beneficial to the long-range lithium diffusion.[20,21,58] In addition, multicationic substitution led to a redistribution of Li over the respective 24*g* and 48*h* sites. Specifically, the 24*g* site occupancy was much increased, thereby decreasing the intercage jump distances. A low activation energy seems to be one of the key features of high entropy Li-ion conductors.[23,71] Taken together, the unique charge-transport characteristics of $Li_{6.5}[P_{0.25}Si_{0.25}Ge_{0.25}Sb_{0.25}]S_5I$ result from a combination of favorable (local) structural changes to the Li sublattice and lattice softening because of the presence of various different elements. The material was also tested as a potential SE for use in bulk-type SSBs with a Ni-rich NCM cathode and LTO anode. However, it was found to be prone to (electro)chemical degradation, even

though the CAM employed was protected by a coating of $LiNbO_3$. The latter prevents direct contact with the SE and usually helps to mitigate interfacial stability problems. The results of this study might pave the way for designing advanced SEs that not only exhibit a high ionic conductivity but are also (electro)chemically stable (essential for practical applications). In particular, we have shown that complex substitution in superionic lithium argyrodites leads to a low activation energy for Li diffusion and further identified specific elemental constituents that negatively affect battery performance. Considering the large compositional space available, multicationic substituted lithium argyrodites can be seen as providing a starting point for tailoring the key properties (by opening up a new playground with infinite possibilities).

Associated content

Supporting information

The Supporting Information is available free of charge on the ACS Publications website at DOI:

Experimental section (incl. details on synthesis, characterization, calculation of configurational entropy, and quantitative XPS analysis), laboratory XRD pattern, structural parameters, Li occupancies, ICP-OES results, additional XPS detail spectra, temperature-dependent diffusion coefficient from ^{7}Li PFG NMR spectroscopy, EIS spectra, and tables showing other compositions targeted in the synthesis, Li-Li jump distances, atomic percentages from quantitative XPS analysis, ionic/electronic conductivities, and activation energies for various lithium argyrodites.

Author information

Corresponding authors

Torsten Brezesinski – Battery and Electrochemistry Laboratory (BELLA), Institute of Nanotechnology, Karlsruhe Institute of Technology (KIT), Hermann-von-Helmholtz-Platz 1, 76344 Eggenstein-Leopoldshafen, Germany; Email: torsten.brezesinski@kit.edu

Florian Strauss – Battery and Electrochemistry Laboratory (BELLA), Institute of Nanotechnology, Karlsruhe Institute of Technology (KIT), Hermann-von-Helmholtz-Platz 1, 76344 Eggenstein-Leopoldshafen, Germany; Email: florian.strauss@kit.edu

Notes

The authors declare no competing financial interest.

Acknowledgment

J.L. acknowledges the Fonds der Chemischen Industrie (FCI) for financial support. F.S. is grateful to the FCI for financial support through a Liebig fellowship. This work was partially supported by BASF SE. The authors thank Dr. Clemens Ritter for collecting the NPD data and Institute Laue-Langevin (ILL) for beamtime allocation under proposal number (5-21-1164) (DOI: 10.5291/ILL-DATA.5-21-1164). Dr. Thomas Bergfeldt is acknowledged for conducting the ICP-OES analysis. TEM data were acquired at the Karlsruhe Nano Micro Facility (KNMFi, www.knmf.kit.edu), a Helmholtz research infrastructure at Karlsruhe Institute of Technology (KIT, www.kit.edu).

References

(1) Myung, S.-T.; Maglia, F.; Park, K.-J.; Yoon, C. S.; Lamp, P.; Kim, S.-J.; Sun, Y.-K. Nickel-Rich Layered Cathode Materials for Automotive Lithium-Ion Batteries: Achievements and Perspectives. *ACS Energy Lett.* **2017**, *2*, 196–223.

(2) Sun, Y.-K. High-Capacity Layered Cathodes for Next-Generation Electric Vehicles. *ACS Energy Lett.* **2019**, *4*, 1042–1044.

(3) Janek, J.; Zeier, W. G. A Solid Future for Battery Development. *Nat. Energy* **2016**, *1*, 16141.

(4) Robinson, A. L.; Janek, J. Solid-State Batteries Enter EV Fray. *Mrs Bull.* **2014**, *39*, 1046–1047.

(5) Kato, Y.; Hori, S.; Saito, T.; Suzuki, K.; Hirayama, M.; Mitsui, A.; Yonemura, M.; Iba, H.; Kanno, R. High-Power All-Solid-State Batteries Using Sulfide Superionic Conductors. *Nat. Energy* **2016**, *1*, 16030.

(6) Lee, Y.-G.; Fujiki, S.; Jung, C.; Suzuki, N.; Yashiro, N.; Omoda, R.; Ko, D.-S.; Shiratsuchi, T.; Sugimoto, T.; Ryu, S.; Ku, J. H.; Watanabe, T.; Park, Y.; Aihara, Y.; Im, D.; Han, I. T. High-Energy Long-Cycling All-Solid-State Lithium Metal Batteries Enabled by Silver–Carbon Composite Anodes. *Nat. Energy* **2020**, *5*, 299–308.

(7) Gao, Z.; Sun, H.; Fu, L.; Ye, F.; Zhang, Y.; Luo, W.; Huang, Y. Promises, Challenges, and Recent Progress of Inorganic Solid-State Electrolytes for All-Solid-State Lithium Batteries. *Adv. Mater.* **2018**, *30*, 1705702.

(8) Lau, J.; DeBlock, R. H.; Butts, D. M.; Ashby, D. S.; Choi, C. S.; Dunn, B. S. Sulfide Solid Electrolytes for Lithium Battery Applications. *Adv. Energy Mater.* **2018**, *8*, 1800933.

(9) Reddy, M. V.; Julien, C. M.; Mauger, A.; Zaghib, K. Sulfide and Oxide Inorganic Solid Electrolytes for All-Solid-State Li Batteries: A Review. *Nanomaterials* **2020**, *10*, 1606.

(10) Zhang, Z.; Shao, Y.; Lotsch, B.; Hu, Y.-S.; Li, H.; Janek, J.; Nazar, L. F.; Nan, C.-W.; Maier, J.; Armand, M.; Chen. L. New Horizons for Inorganic Solid State Ion Conductors. *Energy Environ. Sci.* **2018**, *11*, 1945–1976.

(11) Bai, X.; Duan, Y.; Zhuang, W.; Yang, R.; Wang, J. Research Progress in Li-Argyrodite-Based Solid-State Electrolytes. *J. Mater. Chem. A* **2020**, *8*, 25663–25686.
(12) Yu, C.; Zhao, F.; Luo, J.; Zhang, L.; Sun, X. Recent Development of Lithium Argyrodite Solid-State Electrolytes for Solid-State Batteries: Synthesis, Structure, Stability and Dynamics. *Nano Energy* **2021**, *83*, 105858.
(13) Zhou, L.; Minafra, N.; Zeier, W. G.; Nazar, L. F. Innovative Approaches to Li-Argyrodite Solid Electrolytes for All-Solid-State Lithium Batteries. *Acc. Chem. Res.* **2021**, *54*, 2717–2728.
(14) Deiseroth, H.-J.; Kong, S.-T.; Eckert, H.; Vannahme, J.; Reiner, C.; Zaiß, T.; Schlosser, M. Li_6PS_5X: A Class of Crystalline Li-Rich Solids With an Unusually High Li^+ Mobility. *Angew. Chem. Int. Ed.* **2008**, *47*, 755–758.
(15) Kong, S.-T.; Deiseroth, H.-J.; Reiner, C.; Gün, Ö.; Neumann, E.; Ritter, C.; Zahn, D. Lithium Argyrodites with Phosphorus and Arsenic: Order and Disorder of Lithium Atoms, Crystal Chemistry, and Phase Transitions. *Chem. Eur. J.* **2010**, *16*, 2198–2206.
(16) Zhou, L.; Assoud, A.; Zhang, Q.; Wu, X.; Nazar, L. F. New Family of Argyrodite Thioantimonate Lithium Superionic Conductors. *J. Am. Chem. Soc.* **2019**, *141*, 19002–19013.
(17) Hogrefe, K.; Minafra, N.; Hanghofer, I.; Banik, A.; Zeier, W. G.; Wilkening, H. M. R. Opening Diffusion Pathways through Site Disorder: The Interplay of Local Structure and Ion Dynamics in the Solid Electrolyte $Li_{6+x}P_{1-x}Ge_xS_5I$ as Probed by Neutron Diffraction and NMR. *J. Am. Chem. Soc.* **2022**, *144*, 1795–1812.
(18) Zhao, E.; He, L.; Zhang, Z.; Doux, J.-M.; Tan, D. H. S.; Wu, E. A.; Deysher, G.; Chen, Y.-T.; Zhao, J.; Wang, F.; Meng, Y. S. New Insights into Li Distribution in the Superionic Argyrodite Li_6PS_5Cl. *Chem. Commun.* **2021**, *57*, 10787–10790.
(19) Minafra, N.; Kraft, M. A.; Bernges, T.; Li, C.; Schlem, R.; Morgan, B. J.; Zeier, W. G. Local Charge Inhomogeneity and Lithium Distribution in the Superionic Argyrodites Li_6PS_5X (X = Cl, Br, I). *Inorg. Chem.* **2020**, *59*, 11009–11019.
(20) Kraft, M. A.; Ohno, S.; Zinkevich, T.; Koerver, R.; Culver, S. P.; Fuchs, T.; Senyshyn, A.; Indris, S.; Morgan, B. J.; Zeier, W. G. Inducing High Ionic Conductivity in the Lithium Superionic Argyrodites $Li_{6+x}P_{1-x}Ge_xS_5I$ for All-Solid-State Batteries. *J. Am. Chem. Soc.* **2018**, *140*, 16330–16339.
(21) Ohno, S.; Helm, B.; Fuchs, T.; Dewald, G.; Kraft, M. A.; Culver, S. P.; Senyshyn, A.; Zeier, W. G. Further Evidence for Energy Landscape Flattening in the Superionic Argyrodites $Li_{6+x}P_{1-x}M_xS_5I$ (M = Si, Ge, Sn). *Chem. Mater.* **2019**, *31*, 4936–4944.
(22) Minafra, N.; Culver, S. P.; Krauskopf, T.; Senyshyn, A.; Zeier, W. G. Effect of Si Substitution on the Structural and Transport Properties of Superionic Li-Argyrodites. *J. Mater. Chem. A* **2018**, *6*, 645–651.
(23) Strauss, F.; Lin, J.; Duffiet, M.; Wang, K.; Zinkevich, T.; Hansen, A.-L.; Indris, S.; Brezesinski, T. High-Entropy Polyanionic Lithium Superionic Conductors. *ACS Mater. Lett.* **2022**, *4*, 418–423.

(24) Behera, A. High Entropy Materials. In *Advanced Materials: An Introduction to Modern Materials Science*; Behera, A., Ed.; Springer International Publishing: Cham, **2022**; pp 291–320.
(25) Ma, Y.; Ma, Y.; Wang, Q.; Schweidler, S.; Botros, M.; Fu, T.; Hahn, H.; Brezesinski, T.; Breitung, B. High-Entropy Energy Materials: Challenges and New Opportunities. *Energy Environ. Sci.* **2021**, *14*, 2883–2905.
(26) Sarkar, A.; Breitung, B.; Hahn, H. High Entropy Oxides: The Role of Entropy, Enthalpy and Synergy. *Scr. Mater.* **2020**, *187*, 43–48.
(27) Zhang, R.-Z.; Reece, M. J. Review of High Entropy Ceramics: Design, Synthesis, Structure and Properties. *J. Mater. Chem. A* **2019**, *7*, 22148–22162.
(28) Sarkar, A.; Wang, Q.; Schiele, A.; Chellali, M. R.; Bhattacharya, S. S.; Wang, D.; Brezesinski, T.; Hahn, H.; Velasco, L.; Breitung, B. High-Entropy Oxides: Fundamental Aspects and Electrochemical Properties. *Adv. Mater.* **2019**, *31*, 1806236.
(29) Oses, C.; Toher, C.; Curtarolo, S. High-Entropy Ceramics. *Nat. Rev. Mater.* **2020**, *5*, 295–309.
(30) Lun, Z.; Ouyang, B.; Kwon, D.-H.; Ha, Y.; Foley, E. E.; Huang, T.-Y.; Cai, Z.; Kim, H.; Balasubramanian, M.; Sun, Y.; Huang, J.; Tian, Y.; Kim, H.; McCloskey, B. D.; Yang, W.; Clément, R. J.; Ji, H.; Ceder, G. Cation-Disordered Rocksalt-Type High-Entropy Cathodes for Li-Ion Batteries. *Nat. Mater.* **2021**, *20*, 214–221.
(31) Lin, L.; Wang, K.; Sarkar, A.; Njel, C.; Karkera, G.; Wang, Q.; Azmi, R.; Fichtner, M.; Hahn, H.; Schweidler, S.; Breitung, B. High-Entropy Sulfides as Electrode Materials for Li-Ion Batteries. *Adv. Energy Mater.* **2022**, *12*, 2103090.
(32) Chen, R.; Qiu, P.; Jiang, B.; Hu, P.; Zhang, Y.; Yang, J.; Ren, D.; Shi, X.; Chen, L. Significantly Optimized Thermoelectric Properties in High-Symmetry Cubic Cu_7PSe_6 Compounds *via* Entropy Engineering. *J. Mater. Chem. A* **2018**, *6*, 6493–6502.
(33) Sarkar, A.; Velasco, L.; Wang, D.; Wang, Q.; Talasila, G.; de Biasi, L.; Kübel, C.; Brezesinski, T.; Bhattacharya, S. S.; Hahn, H.; Breitung, B. High Entropy Oxides for Reversible Energy Storage. *Nat. Commun.* **2018**, *9*, 3400.
(34) Zhao, C.; Ding, F.; Lu, Y.; Chen, L.; Hu, Y.-S. High-Entropy Layered Oxide Cathodes for Sodium-Ion Batteries. *Angew. Chem. Int. Ed.* **2020**, *59*, 264–269.
(35) Yang, L.; Chen, C.; Xiong, S.; Zheng, C.; Liu, P.; Ma, Y.; Xu, W.; Tang, Y.; Ong, S. P.; Chen, H. Multiprincipal Component P2-$Na_{0.6}(Ti_{0.2}Mn_{0.2}Co_{0.2}Ni_{0.2}Ru_{0.2})O_2$ as a High-Rate Cathode for Sodium-Ion Batteries. *JACS Au* **2021**, *1*, 98–107.
(36) Fu, F.; Liu, X.; Fu, X.; Chen, H.; Huang, L.; Fan, J.; Le, J.; Wang, Q.; Yang, W.; Ren, Y.; Amine, K.; Sun, S.-G.; Xu, G.-L. Entropy and Crystal-Facet Modulation of P2-Type Layered Cathodes for Long-Lasting Sodium-Based Batteries. *Nat. Commun.* **2022**, *13*, 2826.
(37) Ma, Y.; Hu, Y.; Pramudya, Y.; Diemant, T.; Wang, Q.; Goonetilleke, D.; Tang, Y.; Zhou, B.; Hahn, H.; Wenzel, W.; Fichtner, M.; Ma, Y.; Breitung, B.; Brezesinski, T. Resolving the Role of Configurational Entropy in Improving Cycling

Performance of Multicomponent Hexacyanoferrate Cathodes for Sodium-Ion Batteries. *Adv. Funct. Mater.* **2022**, *32*, 2202372.

(38) Ma, Y.; Ma, Y.; Dreyer, S. L.; Wang, Q.; Wang, K.; Goonetilleke, D.; Omar, A.; Mikhailova, D.; Hahn, H.; Breitung, B.; Brezesinski, T. High-Entropy Metal–Organic Frameworks for Highly Reversible Sodium Storage. *Adv. Mater.* **2021**, *33*, 2101342.

(39) Wang, J.; Cui, Y.; Wang, Q.; Wang, K.; Huang, X.; Stenzel, D.; Sarkar, A.; Azmi, R.; Bergfeldt, T.; Bhattacharya, S. S.; Kruk, R.; Hahn, H.; Schweidler, S.; Brezesinski, T.; Breitung, B. Lithium Containing Layered High Entropy Oxide Structures. *Sci. Rep.* **2020**, *10*, 18430.

(40) Harm, S.; Hatz, A.-K.; Moudrakovski, I.; Eger, R.; Kuhn, A.; Hoch, C.; Lotsch, B. V. Lesson Learned from NMR: Characterization and Ionic Conductivity of LGPS-like Li_7SiPS_8. *Chem. Mater.* **2019**, *31*, 1280–1288.

(41) Dietrich, C.; Sadowski, M.; Sicolo, S.; Weber, D. A.; Sedlmaier, S. J.; Weldert, K. S.; Indris, S.; Albe, K.; Janek, J.; Zeier, W. G. Local Structural Investigations, Defect Formation, and Ionic Conductivity of the Lithium Ionic Conductor $Li_4P_2S_6$. *Chem. Mater.* **2016**, *28*, 8764–8773.

(42) Lee, Y.; Jeong, J.; Lee, H. J.; Kim, M.; Han, D.; Kim, H.; Yuk, J. M.; Nam, K.-W.; Chung, K. Y.; Jung, H.-G.; Yu, S. Lithium Argyrodite Sulfide Electrolytes with High Ionic Conductivity and Air Stability for All-Solid-State Li-Ion Batteries. *ACS Energy Lett.* **2022**, *7*, 171–179.

(43) Zakaznova-Herzog, V. P.; Harmer, S. L.; Nesbitt, H. W.; Bancroft, G. M.; Flemming, R.; Pratt, A. R. High Resolution XPS Study of the Large-Band-Gap Semiconductor Stibnite (Sb_2S_3): Structural Contributions and Surface Reconstruction. *Surf. Sci.* **2006**, *600*, 348–356.

(44) Wang, L.; Yang, B.; Xia, Z.; Leng, M.; Zhou, Y.; Xue, D.-J.; Zhong, J.; Gao, L.; Song, H.; Tang, J. Synthesis and Characterization of Hydrazine Solution Processed $Cu_{12}Sb_4S_{13}$ Film. *Sol. Energy Mater. Sol. Cells* **2016**, *144*, 33–39.

(45) Avilez Garcia, R. G.; Meza Avendaño, C. A.; Pal, M.; Paraguay Delgado, F.; Mathews, N. R. Antimony Sulfide (Sb_2S_3) Thin Films by Pulse Electrodeposition: Effect of Thermal Treatment on Structural, Optical and Electrical Properties. *Mater. Sci. Semicond. Process.* **2016**, *44*, 91–100.

(46) Teo, J. H.; Strauss, F.; Walther, F.; Ma, Y.; Payandeh, S.; Scherer, T.; Bianchini, M.; Janek, J.; Brezesinski, T. The Interplay between (Electro)Chemical and (Chemo)Mechanical Effects in the Cycling Performance of Thiophosphate-Based Solid-State Batteries. *Mater. Futures* **2022**, *1,* 015102.

(47) Ma, Y.; Teo, J. H.; Kitsche, D.; Diemant, T.; Strauss, F.; Ma, Y.; Goonetilleke, D.; Janek, J.; Bianchini, M.; Brezesinski, T. Cycling Performance and Limitations of $LiNiO_2$ in Solid-State Batteries. *ACS Energy Lett.* **2021**, *6*, 3020–3028.

(48) Auvergniot, J.; Cassel, A.; Ledeuil, J.-B.; Viallet, V.; Seznec, V.; Dedryvère, R. Interface Stability of Argyrodite Li_6PS_5Cl toward $LiCoO_2$, $LiNi_{1/3}Co_{1/3}Mn_{1/3}O_2$, and $LiMn_2O_4$ in Bulk All-Solid-State Batteries. *Chem. Mater.* **2017**, *29*, 3883–3890.

(49) Liang, J.; Li, X.; Zhao, Y.; Goncharova, L. V.; Li, W.; Adair, K. R.; Banis, M. N.; Hu, Y.; Sham, T.-K.; Huang, H.; Zhang, L.; Zhao, S.; Lu, S.; Li, R.; Sun, X. An Air-Stable and Dendrite-Free Li Anode for Highly Stable All-Solid-State Sulfide-Based Li Batteries. *Adv. Energy Mater.* **2019**, *9*, 1902125.

(50) Foix, D.; Gonbeau, D.; Taillades, G.; Pradel, A.; Ribes, M. The Structure of Ionically Conductive Chalcogenide Glasses: A Combined NMR, XPS and Ab Initio Calculation Study. *Solid State Sci.* **2001**, *3*, 235–243.

(51) Ingo, G. M.; Dirè, S.; Babonneau, F. XPS Studies of SiO_2-TiO_2 Powders Prepared by Sol-Gel Process. *Appl. Surf. Sci.* **1993**, *70–71*, 230–234.

(52) Tunc, I.; Suzer, S.; Correa-Duarte, M. A.; Liz-Marzán, L. M. XPS Characterization of Au (Core)/SiO_2 (Shell) Nanoparticles*. J. Phys. Chem. B* **2005**, *109,* 7597–7600.

(53) Kim, S.; Kim, S.-K.; Sun, P.; Oh, N.; Braun, P. V. Reduced Graphene Oxide/LiI Composite Lithium Ion Battery Cathodes. *Nano Lett.* **2017**, *17*, 6893–6899.

(54) Strydom, C. A.; van Staden, J. F.; Strydom, H. J. An XPS Investigation of the Influence of Bromide and Iodide Solutions on the Surface of Silver Chloride Coated Ion-Selective Electrodes. *Electroanalysis* **1991**, *3*, 197–201.

(55) Zhang, W.; Leichtweiß, T.; Culver, S. P.; Koerver, R.; Das, D.; Weber, D. A.; Zeier, W. G.; Janek, J. The Detrimental Effects of Carbon Additives in $Li_{10}GeP_2S_{12}$-Based Solid-State Batteries. *ACS Appl. Mater. Interfaces* **2017**, *9*, 35888–35896.

(56) Zhang, W.; Richter, F. H.; Culver, S. P.; Leichtweiss, T.; Lozano, J. G.; Dietrich, C.; Bruce, P. G.; Zeier, W. G.; Janek, J. Degradation Mechanisms at the $Li_{10}GeP_2S_{12}$/$LiCoO_2$ Cathode Interface in an All-Solid-State Lithium-Ion Battery*. ACS Appl. Mater. Interfaces*. **2018**, *10,* 22226–22236.

(57) Mori, D.; Oka, H.; Hosoi, T.; Kawai, K.; Morita, M.; Crumlin, E. J.; Liu, Z.; Watanabe, H.; Arima, K. Comparative Study of GeO_2/Ge and SiO_2/Si Structures on Anomalous Charging of Oxide Films upon Water Adsorption Revealed by Ambient-Pressure X-Ray Photoelectron Spectroscopy. *J. Appl. Phys.* **2016**, *120*, 095306.

(58) Adeli, P.; Bazak, J. D.; Park, K. H.; Kochetkov, I.; Huq, A.; Goward, G. R.; Nazar, L. F. Boosting Solid-State Diffusivity and Conductivity in Lithium Superionic Argyrodites by Halide Substitution. *Angew. Chem. Int. Ed.* **2019**, *58*, 8681–8686.

(59) Kuhn, A.; Duppel, V.; Lotsch, B. V. Tetragonal $Li_{10}GeP_2S_{12}$ and Li_7GePS_8 – Exploring the Li Ion Dynamics in LGPS Li Electrolytes. *Energy Environ. Sci.* **2013**, *6*, 3548–3552.

(60) Kuhn, A.; Gerbig, O.; Zhu, C.; Falkenberg, F.; Maier, J.; Lotsch, B. V. A New Ultrafast Superionic Li-Conductor: Ion Dynamics in $Li_{11}Si_2PS_{12}$ and Comparison with Other Tetragonal LGPS-Type Electrolytes. *Phys. Chem. Chem. Phys.* **2014**, *16*, 14669–14674.

(61) Sedlmaier, S. J.; Indris, S.; Dietrich, C.; Yavuz, M.; Dräger, C.; von Seggern, F.; Sommer, H.; Janek, J. Li_4PS_4I: A Li^+ Superionic Conductor Synthesized by a Solvent-Based Soft Chemistry Approach. *Chem. Mater.* **2017**, *29*, 1830–1835.

(62) Strauss, F.; Zinkevich, T.; Indris, S.; Brezesinski, T. Li_7GeS_5Br–An Argyrodite Li-Ion Conductor Prepared by Mechanochemical Synthesis. *Inorg. Chem.* **2020**, *59*, 12954–12959.

(63) Walther, F.; Randau, S.; Schneider, Y.; Sann, J.; Rohnke, M.; Richter, F. H.; Zeier, W. G.; Janek, J. Influence of Carbon Additives on the Decomposition Pathways in Cathodes of Lithium Thiophosphate-Based All-Solid-State Batteries. *Chem. Mater.* **2020**, *32*, 6123–6136.

(64) Walther, F.; Koerver, R.; Fuchs, T.; Ohno, S.; Sann, J.; Rohnke, M.; Zeier, W. G.; Janek, J. Visualization of the Interfacial Decomposition of Composite Cathodes in Argyrodite-Based All-Solid-State Batteries Using Time-of-Flight Secondary-Ion Mass Spectrometry. *Chem. Mater.* **2019**, *31,* 3745–3755.

(65) Bartsch, T.; Strauss, F.; Hatsukade, T.; Schiele, A.; Kim, A-Y.; Hartmann, P.; Janek, J.; Brezesinski, T. Gas Evolution in All-Solid-State Battery Cells. *ACS Energy Lett.* **2018**, *3*, 2539–2543.

(66) Kim, A-Y.; Strauss, F.; Bartsch, T.; Teo, J. H.; Hatsukade, T.; Mazilkin, A.; Janek, J.; Hartmann, P.; Brezesinski, T. Stabilizing Effect of a Hybrid Surface Coating on a Ni-Rich NCM Cathode Material in All-Solid-State Batteries. *Chem. Mater.* **2019**, *31,* 9664–9672.

(67) Strauss, F.; Teo, J. H.; Maibach, J.; Kim, A-Y.; Mazilkin, A.; Janek, J.; Brezesinski, T. Li_2ZrO_3-Coated NCM622 for Application in Inorganic Solid-State Batteries: Role of Surface Carbonates in the Cycling Performance. *ACS Appl. Mater. Interfaces* **2020**, *12*, 57146–57154.

(68) Strauss, F.; Payandeh, S.; Kondrakov, A.; Brezesinski, T. On the Role of Surface Carbonate Species in Determining the Cycling Performance of All-Solid-State Batteries. *Mater. Futures* **2022**, *1,* 023501.

(69) Koerver, R.; Walther, F.; Aygün, I.; Sann, J.; Dietrich, C.; Zeier, W. G.; Janek, J. Redox-Active Cathode Interphases in Solid-State Batteries. *J. Mater. Chem. A* **2017**, *5*, 22750–22760.

(70) Auvergniot, J.; Cassel, A.; Foix, D.; Viallet, V.; Seznec, V.; Dedryvère, R. Redox Activity of Argyrodite Li_6PS_5Cl Electrolyte in All-Solid-State Li-Ion Battery: An XPS Study. *Solid State Ion.* **2017**, *300*, 78–85.

(71) Zhao, G.; Suzuki, K.; Okumura, T.; Takeuchi, T.; Hirayama, M.; Kanno, R. Extending the Frontiers of Lithium-Ion Conducting Oxides: Development of Multicomponent Materials with γ-Li_3PO_4-Type Structures. *Chem. Mater.* **2022**, *34,* 3948–3959.

TOC graphic